JGR Planets

RESEARCH ARTICLE
10.1029/2021JE007015

**Key Points:**

- Thermal properties of liquid iron are determined up to 3.0 TPa and 25000 K using the formally exact ab initio thermodynamic integration
- Temperature of a completely molten core can be twice of a frozen core whereas the core pressures are similar
- Crystallization of the cores of massive planets proceeds from the bottom-up rather than the top-down

**Supporting Information:**

Supporting Information may be found in the online version of this article.

**Correspondence to:**

T. Sun,
tsun@ucas.ac.cn

**Citation:**

Li, Q., Xian, J.-W., Zhang, Y., Sun, T., & Vočadlo, L. (2022). Thermal properties of liquid iron at conditions of planetary cores. *Journal of Geophysical Research: Planets*, *127*, e2021JE007015. https://doi.org/10.1029/2021JE007015

Received 29 SEP 2021
Accepted 30 MAR 2022



# Thermal Properties of Liquid Iron at Conditions of Planetary Cores

**Qing Li[1], Jia-Wei Xian[2], Yigang Zhang[1], Tao Sun[1], and Lidunka Vočadlo[3]**

[1]Key Laboratory of Computational Geodynamics, College of Earth and Planetary Sciences, University of Chinese Academy of Sciences, Beijing, China, [2]Laboratory of Computational Physics, Institute of Applied Physics and Computational Mathematics, Beijing, China, [3]Department of Earth Sciences, University College London, London, UK

**Abstract** Thermal properties of iron at high pressures ($P$) and temperatures ($T$) are essential for determining the internal structure and evolution of planetary cores. Compared to its solid counterpart, the liquid phase of iron is less studied and existing results exhibit large discrepancies, hindering a proper understanding of planetary cores. Here we use the formally exact *ab initio* thermodynamic integration approach to calculate thermal properties of liquid iron up to 3.0 TPa and 25000 K. Uncertainties associated with theory are compensated by introducing a $T$-independent pressure shift based on experimental data. The resulting thermal equation of state agrees well with the diamond anvil cell (DAC) data in the $P$-$T$ range of measurements. At higher $P$-$T$ it matches the reduced shock wave data yet deviates considerably from the extrapolations of DAC measurements, indicating the latter may require further examinations. Moreover, the calculated heat capacity and thermal expansivity are substantially lower than some recent reports, which have important ramifications for understanding thermal evolutions of planetary cores. Using Kepler-36b as a prototype, we examine how a completely molten core may affect the $P$-$T$ profiles of massive exoplanets. By comparing the melting slope and the adiabatic slope along the iron melting line, we propose that crystallization of the cores of massive planets proceeds from the bottom-up rather than the top-down.

**Plain Language Summary** Earth-like planets often possess iron-dominant cores that are partially or completely molten. The thermal properties of liquid iron are therefore essential to constrain the internal pressure, temperature, and evolution of planets. However, existing studies on the topic are limited and the results exhibit large discrepancies, hindering a proper understanding of planetary cores. Here, we simulate the thermal properties of liquid iron using *ab initio* thermodynamics integration, a formally exact free-energy method that is well suited to determine thermal properties. This method achieves highly accurate results at extreme pressure and temperature conditions. Our results help to constrain the pressure-temperature profiles and thermal evolutions of Earth-like planets, from smaller ones such as Mars and Mercury to massive exoplanets where the core pressures may exceed 2 TPa. The calculated heat capacity and thermal expansivity are substantially lower than in previous studies, indicating smaller thermal inertia and more rapid core evolution. Core crystallization in massive planets may proceed from the bottom-up, in contrast to the smaller terrestrial planets of the Solar System.

## 1. Introduction

Iron is the dominant element in the cores of terrestrial planets (de Pater & Lissauer, 2015). For Earth it comprises ~90 wt% of its liquid outer core and ~97 wt% of solid inner core (Stacey & Davis, 2008). Similar proportions of iron may also be present in the cores of smaller rocky planets like Mercury (Chabot et al., 2014) or more massive exoplanets cataloged as super Earths (Boujibar et al., 2020). Accordingly, thermal properties of iron at high pressures ($P$) and temperatures ($T$) are of great significance in Earth and planetary sciences. For instance, thermal equations of states (EoS) of iron are essential for building internal structure models of planets (Anderson & Ahrens, 1994; Dorogokupets et al., 2017; Fei et al., 2016; Komabayashi, 2014; Miozzi et al., 2020). The adiabatic slope $(dT/dP)_s \equiv \frac{\alpha T}{\rho C_p}$, with $\alpha$ thermal expansivity, $\rho$ density, $C_p$ isobaric heat capacity, determines the core's temperature profile (Boujibar et al., 2020; Grant et al., 2021). Thermal properties of iron are also vital to understand the evolution of the core and the dynamo responsible for the planet's magnetic field (Bonati et al., 2021; Gaidos et al., 2010). Even though iron cannot be the sole element in planetary cores, using pure iron to model the cores provides a primary framework from which more realistic models can be constructed.

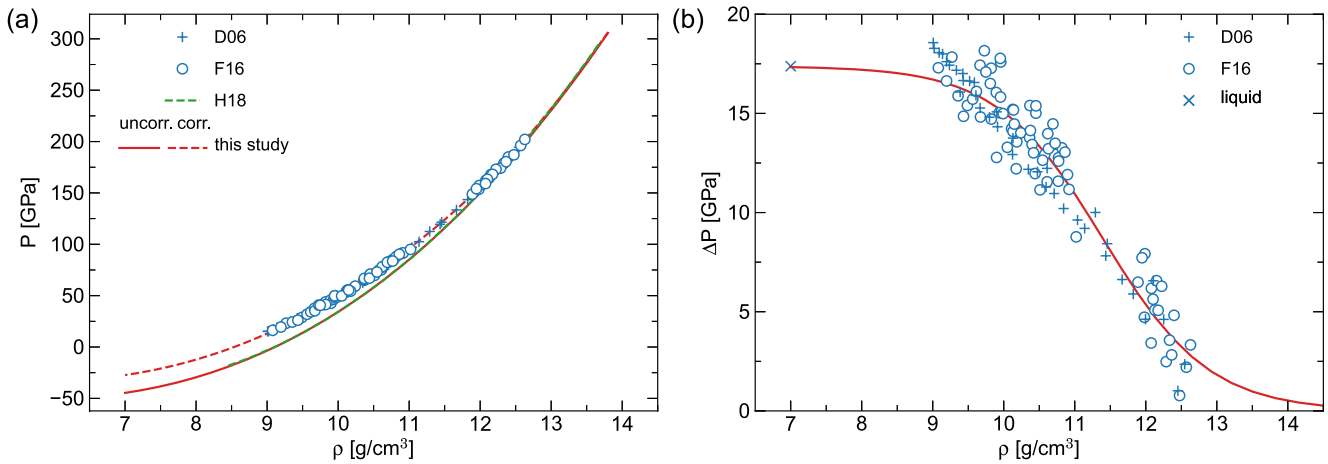


**Figure 1.** Pressure correction to *ab initio* simulations of liquid iron. (a) Static equations of states (EoS) of hcp iron determined by *ab initio* simulations versus experiments. "D06" and "F16" denote the experimental data of Dewaele et al. (2006) and Fei et al. (2016), "H18" denotes the *ab initio* calculation by Hakim et al. (2018), "this study" represent the EoS of hcp iron from our calculation before ("uncor.") and after pressure shift ("cor."). As the original experiments were conducted at 300 K, a thermal pressure of 2.5 GPa (Murphy et al., 2011) was subtracted to get the static pressure. (b) Pressure differences between *ab initio* simulations and experiments. They are fitted to a sigmoid function $\Delta P(\rho) = 17.38/(1 + \exp((\rho - 11.395) \cdot 1.341))$, with $\Delta P$ in the unit of GPa, $\rho$ in the unit of g/cm$^3$.

Iron has a lower melting temperature than typical mantle minerals (Stixrude, 2014). As a result it is likely to exist in the liquid phase through the major stages of planetary evolution (Margot et al., 2007; Rubie et al., 2015; Stähler et al., 2021). Yet compared to the solid phase of iron, liquid iron is less studied, especially in the TPa regime important for massive exoplanets. Accordingly, planetary modeling of internal structures is often restricted to frozen cores (Hakim et al., 2018; Smith et al., 2018). The *P-T* profiles of massive rocky planets with molten cores remain unclear (Unterborn & Panero, 2019). The relative scarcity of studies on the liquid phase may be related to its inherent high *T*, which makes experiments more challenging. Also, the liquid phase lacks long-range ordering and extracting its density from X-ray diffraction becomes difficult. Only recently these difficulties were overcome and the *P-ρ-T* relation of liquid iron was measured directly via diamond anvil cell (DAC) experiments in the range of 20–135 GPa, 2600–4200 K (Kuwayama et al., 2020). Higher *P-T* conditions have been reached via shock (Al'tshuler et al., 1996; Brown et al., 2000) or ramp (Grant et al., 2021) compressions. However the EoS reduced from shock wave data (Anderson & Ahrens, 1994; Brown & Mcqueen, 1986) differs considerably from the extrapolation of DAC measurements (Kuwayama et al., 2020). For instance, extrapolation of DAC measurements indicates that at 12.64 g/cm$^3$ and 5000 K, liquid iron has a pressure of 278 GPa. Yet to reach the same pressure at this density, shock wave reduction predicts a temperature ~900 K higher (Anderson & Ahrens, 1994) or more (Brown & Mcqueen, 1986). Complementary to experiments, thermal properties of liquid iron can also be determined via ab initio molecular dynamics (AIMD) simulations based on density functional theory (DFT). Such simulations have been used to determine properties of liquid iron at conditions of the Earth's outer core (Alfè et al., 2000, 2002; Ichikawa et al., 2014; Vočadlo et al., 2003) as well as those of warm dense matter (Sjostrom & Crockett, 2018). More recently, Wagle and Steinle-Neumann (2019) used AIMD combined with an empirical correction to construct an EOS of liquid iron up to conditions of super-Earths. These simulations were conducted without considering the iron 3*s* as valence electrons. Accordingly, pressure was limited to 1.5 TPa, 1 TPa lower than the upper-bound estimated for massive super-Earths (Unterborn & Panero, 2019). Moreover, the reported thermodynamic properties such as heat capacity and thermal expansivity are substantially higher than previous studies. For instance, $C_p$ under conditions of the Earth's outer core (136–330 GPa, 4000–6000 K) was determined as ~1200 J/(kg·K), more than 50% higher than ~700 J/(kg·K) by Anderson and Ahrens (1994) or ~800 J/(kg·K) by Stacey and Davis (2008). Such large discrepancies undermine a proper understanding of the thermal evolution of planetary cores (Buffett et al., 1992) and need to be resolved.

Here we calculate thermal properties of liquid iron at conditions of planetary cores using *ab initio* thermodynamic integration (TI). TI is a formally exact free energy method and well suited to get highly accurate thermal properties (Sun et al., 2018). The iron 3*s* electrons were treated as valence electrons, allowing us to extend the pressure range to 3 TPa. It turns out the effect of 3*s* electrons increases with *T* and needs to be taken into account even at relatively low pressures. We then apply these results to tackle three pending problems in planetary sciences: (a) thermal properties of

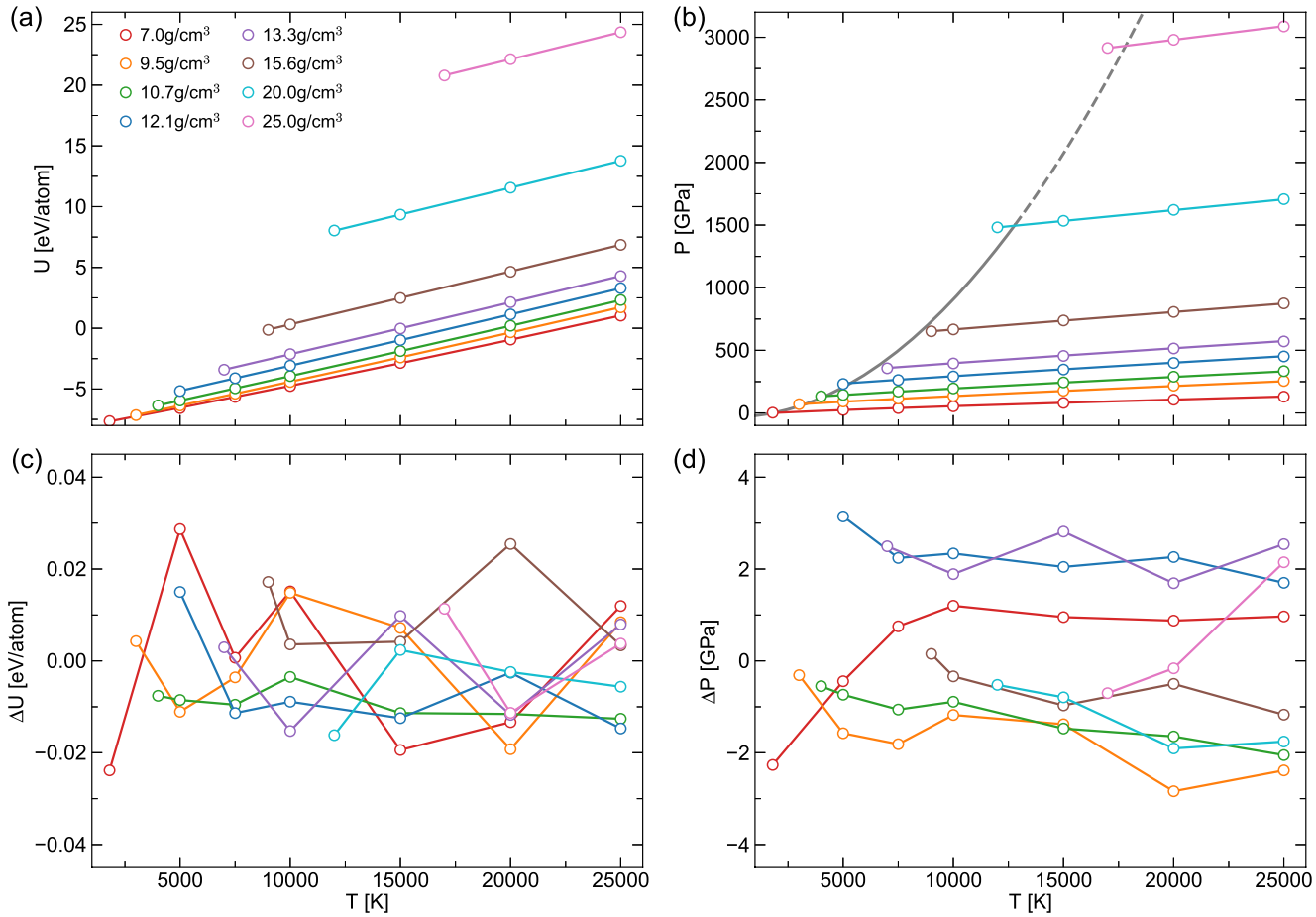


**Figure 2.** (a) Internal energies and (b) pressures of liquid iron after pressure correction. Open circles and the associated solid lines denote the ab initio molecular dynamics results with fittings using Equations 1 and 4. (c) Fitting errors of internal energy and (d) pressure. Data points of the same density are connected by lines. The gray solid (dashed) line in (b) denotes the calculated (extrapolated) iron melting curve by Bouchet et al. (2013), $T_m = 1811(P/31.3 + 1)^{1/1.99}$, with $T_m$ in the unit of Kelvin, $P$ in the unit of GPa.

the Earth's outer core. (b) The temperature and pressure profiles of a massive exoplanet with a completely molten core, (c) whether a molten planetary core crystallizes from the bottom-up, from the top-down, or something more complex.

**Table 1**
*Parameters (in eV) for the Helmholtz Free Energy of Liquid Iron*

| | $c_{ij}$ | | | |
|---|---|---|---|---|
| $j$ | $i = 0$ | $i = 1$ | $i = 2$ | $d_j$ |
| 0 | −6.33398 | 4.15051 | 0.04097 | −15.35200 |
| 1 | 33.15671 | 2.82654 | −0.36173 | 51.89954 |
| 2 | 145.08894 | −4.00514 | −0.30364 | 124.67947 |
| 3 | 95.85711 | 1.28082 | 0.19107 | 97.72656 |
| 4 | −75.13252 | −122.99523 | 34.88034 | −153.06548 |

## 2. Thermodynamic Modeling

Thermal properties of a single phase material are fully determined by its Helmholtz free energy $F(V, T)$, where $F(V, T)$ is a continuous function of volume $V$ and temperature $T$. Yet ab initio molecular dynamics (AIMD) simulations are conducted on a discrete $V_n$-$T_n$ grid with time-averaged internal energy $U_n$ and pressure $P_n$ as outputs. The subscript $n$ enumerates the individual AIMD simulations. To proceed from discrete ($U_n$, $P_n$, $V_n$, $T_n$) to continuous $F(V, T)$, some form of thermodynamic modeling is essential. The main challenge is to find simple functions that can fit the data accurately over a wide $V$-$T$ range, while at the same time ensure the model is thermodynamically self-consistent. Here we represent the internal energy per atom $U$ as

$$U = \sum_{i=0}^{2} \sum_{j=0}^{4} c_{ij} t^i f^j, \quad (1)$$

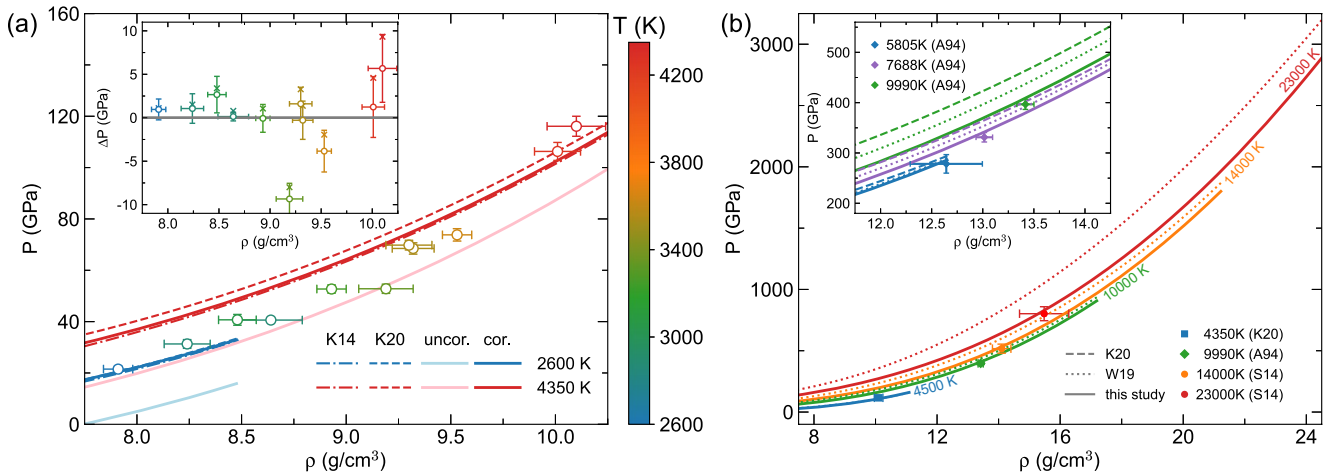


**Figure 3.** (a) Thermal equations of states (EoS) of liquid iron in the $\rho$-$T$ range of the diamond anvil cell experiment of Kuwayama et al. (2020). Open circles with error bars denote the original measurements. The associated thermal EoS are denoted by dashed lines (labeled as "K20"). Solid lines represent the EoS from our calculations, with ("cor.") and without pressure shift ("uncor."). Inset: the pressure difference between the original measurements and the EoS of Kuwayama et al. (2020) (open circles) and the present study after pressure shift (crosses). The two EoS agree with the original measurements equally well. (b) Thermal EoS of liquid iron in the whole $\rho$-$T$ range explored by the present study. "K14" denotes the results of thermodynamic modeling by Komabayashi (2014). "K20" denotes the DAC results of Kuwayama et al. (2020). "A94" and "S14" denotes the reduced shock data from Anderson and Ahrens (1994) and Sakaiya et al. (2014), respectively. "W19" denotes the density functional theory results of Wagle and Steinle-Neumann (2019). Inset: detailed comparison with the reduced shock data of Anderson and Ahrens (1994).

where $t = T/T_0$, $f = \frac{1}{2}\left[\left(\frac{V_0}{V}\right)^{\frac{2}{3}} - 1\right]$, $c_{ij}$ are fitting parameters, $T_0$ and $V_0$ are the temperature and volume of the reference state. Here we choose $T_0 = 10000\ K$ and $V_0 = 6.97\ \text{Å}^3$/atom ($\rho_0 = 13.3$ g/cm$^3$). The Helmholtz free energy per atom $F$ can then be determined from the thermodynamic relation $F/T - F_0/T_0 = -\int_{T_0}^{T} U/T^2 dT$ as

$$F = -\sum_{i\neq 1}^{2}\sum_{j=0}^{4} c_{ij}\frac{t^i - t}{i-1}f^j - \sum_{j=0}^{4} c_{1j} f^j t\ln t + F_0 t, \tag{2}$$

where $F_0$ denotes the Helmholtz free energy at $T_0$ and is expressed as

$$F_0 = \sum_{j=0}^{4} d_j f^j, \tag{3}$$

with $d_j$ another set of fitting parameters. The pressure $P$ is determined from $P = -(\partial F/\partial V)_T$ as

$$P = \left(\sum_{i\neq 1}^{2}\sum_{j=1}^{4} c_{ij}\frac{t^i - t}{i-1} j f^{j-1} + \sum_{j=1}^{4} c_{1j} j f^{j-1} t\ln t - \sum_{j=1}^{4} d_j j f^{j-1} t\right)\frac{df}{dV}, \tag{4}$$

where $\frac{df}{dV} = -\frac{(2f+1)^{\frac{5}{2}}}{3V_0}$.

Fitting the discrete ($U_n$, $P_n$, $V_n$, $T_n$) from AIMD allows us to determine all the $c_{ij}$ and $d_j$ except $d_0$, which corresponds to a constant entropy term. This term is fixed by a separate ab initio TI calculation. Thermal properties of the system at arbitrary ($V$, $T$) can then be determined from a single Helmholtz function (Equation 2). As such, the model is thermodynamically self-consistent.

## 3. Simulation Details

The AIMD simulations were performed in the *NVT* ensemble via the Vienna Ab initio Simulation Package (Kresse & Furthmüller, 1996; Kresse & Hafner, 1994; Kresse & Joubert, 1999). The electron-electron exchange-correlation interaction was approximated with the generalized-gradient approximation as parametrized

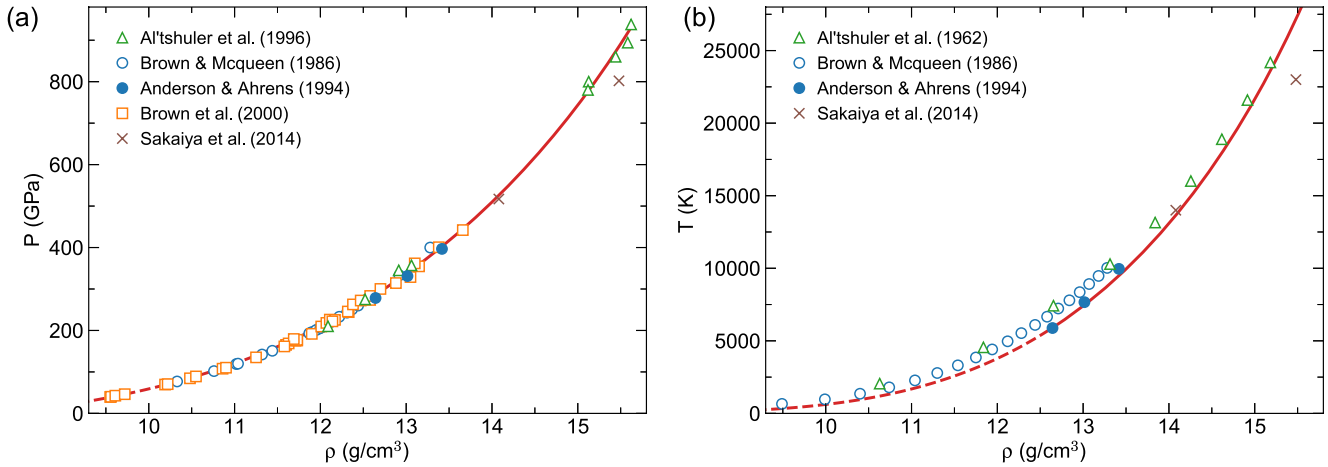


**Figure 4.** Shock Hugoniot of liquid iron: (a) the Hugoniot pressure (b) the Hugoniot temperature. Along the Hugoniot, the solid-liquid phase transition takes place at about 12.6 g/cm$^3$ (Anderson & Ahrens, 1994). We thus use solid (dashed) lines to denote the Hugoniot where iron is in liquid (solid) phase.

by Perdew, Burke and Ernzerhof (PBE) (Perdew et al., 1996). Because of the high pressure and temperature involved, we chose a projector augmented-wave (PAW) pseudopotential (Blöchl, 1994) containing 16 valence electrons [$3s^2 3p^6 3d^7 4s^1$]. This pseudopotential has a core radius of 1.9 a.u.. The predictions it makes agree well with those from all electron simulations as well as a PAW pseudo-potential with a smaller core-radius (1.5 a.u.) using the *Quantum-Espresso* code (Giannozzi et al., 2009), indicating this pseudo-potential is appropriate for the present study (Li et al., 2021). The kinetic energy cutoff for the plane wave expansion was set to 650 eV and the Brillouin zone sampling was limited to the Gamma point only. The cubic simulation cell contained 108 atoms with the ionic temperature controlled by a Nosé thermostat (Nosé, 1984), whereas electronic thermal excitations were treated by minimizing the Mermin functional (Mermin, 1965). Tests on a larger cell with 216 atoms indicate that the size effects on thermal properties are negligible (Li et al., 2021). The convergence threshold for electronic self-consistent field minimization was set to $10^{-5}$ eV to get accurate Hellman-Feynman forces, which, along with a time step of 1 fs, ensured the dynamics of the system was faithfully represented in AIMD trajectories. To facilitate thermal equilibration, simulations were arranged in the order of decreasing temperatures, with the last configuration from the prior simulation serving as the initial configuration of the present simulation. Each simulation ran 0.5–1 ps for thermal equilibration, then another 10 ps for production with time-averaged energy and pressure as outputs.

The energy and pressure results from the above procedure correspond to a "coarse" setting where the kinetic energy cutoff for the plane wave expansion was 650 eV and the Brillouin zone sampling was limited to the Gamma point only. To ensure convergence, we randomly selected 20 snapshots along AIMD trajectories and recalculated their energies and pressures using a higher kinetic energy cutoff of 850 eV and a denser $2 \times 2 \times 2$ k-mesh sampling. The differences (see Table S1 in Supporting Information S1) were then added to the energy and pressure data from the coarse setting to get the fully converged ($U_n$, $P_n$, $V_n$, $T_n$).

The ($U_n$, $P_n$, $V_n$, $T_n$) from the above procedure can only constrain $F(V, T)$ up to a constant entropy term. To determine the absolute entropy of system and fix the parameter $d_0$ in Equation 3, we employed a recently developed *ab initio* TI approach (Sun et al., 2018). In this approach, a Weeks-Chandler-Andersen (WCA) gas was chosen as the reference system whose free energy was known (Heyes & Okumura, 2006; Mirzaeinia et al., 2017). Then, a series of simulations were performed with interatomic interaction

$$\Phi_\lambda = \Phi_{\mathrm{WCA}} + \lambda\Phi, \tag{5}$$

where $\Phi$ is the *ab initio* electronic free energy, $\Phi_{\mathrm{WCA}}$ is the potential energy of the WCA gas, $\lambda$ is the coupling constant. The free energy difference between the WCA gas and the ab initio system was then determined via $\int_0^1 \langle\Phi\rangle_\lambda d\lambda$.

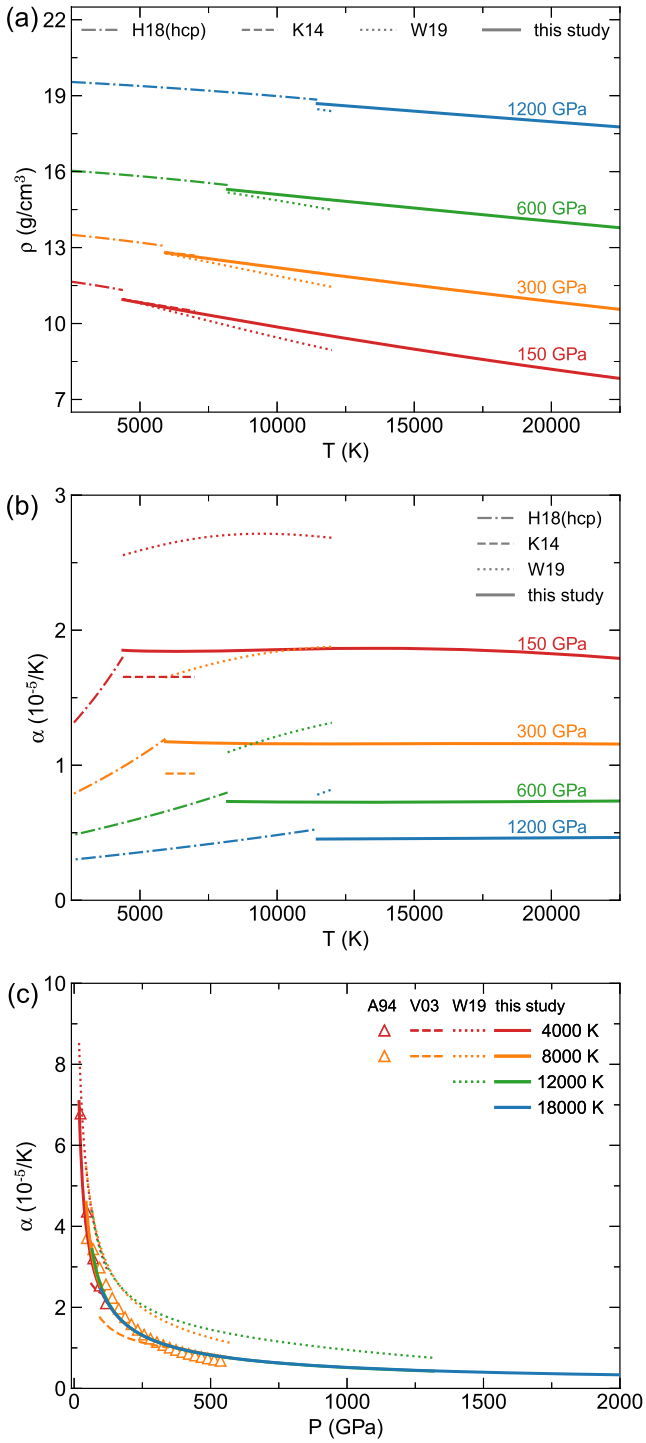


**Figure 5.** (a) Density of liquid iron as a function of temperature. (b) Thermal expansivity of liquid iron as a function of temperature. (c) Thermal expansivity of liquid iron as a function of pressure. For comparison properties of hcp iron ["H18" by Hakim et al. (2018)] are also shown. "A94" denotes thermal properties of liquid iron from the reduced shock data by Anderson and Ahrens (1994). "K14" denotes the results of thermodynamic modeling by Komabayashi (2014). "V03" and "W19" denote the density functional theory results for liquid iron by Vočadlo et al. (2003) and Wagle and Steinle-Neumann (2019).

## 4. Pressure Shift

At low densities, *ab initio* simulations cannot describe the EoS of iron very well (Alfè et al., 2002; Edgington et al., 2019). Near ambient melting point (7.02 g/cm$^3$, 1811 K), our calculated pressure is about ~17 GPa, whereas the experimental pressure is zero. This discrepancy is partly caused by the intrinsic error in the PBE functional. It is also related to the fact that our simulations are non spin-polarized whereas liquid iron is paramagnetic at low *P-T* (Waseda & Suzuki, 1970). To overcome these deficiencies, a common practice is to introduce a temperature-independent pressure shift $\Delta P_c$ which brings simulation results closer to experiments (Alfè et al., 2002; Badro et al., 2014; Umemoto & Hirose, 2020; Wagle & Steinle-Neumann, 2019). In the work of Wagle and Steinle-Neumann (2019), $\Delta P_c$ was determined from the experimentally measured triple-point of iron and the thermal expansivity $\alpha$ at the ambient melting point. However due to the large uncertainties associated with $\alpha$, $\Delta P_c$ remains somewhat indeterminate. Here we take a different approach. We note both liquid iron and the hexagonal close packed (hcp) iron are close packed structures with similar coordination numbers (Alfè et al., 2000), their $\Delta P_c$ are likely to be similar. We thus determine $\Delta P_c$ by comparing the theoretical static EoS of hcp iron with that of experiments (Dewaele et al., 2006; Fei et al., 2016), as shown in Figure 1a. A caveat here is the hcp iron is unstable below 20 GPa and the relevant experimental data is absent in this pressure range. Yet the density of liquid iron at the ambient melting point has been accurately determined (Anderson & Ahrens, 1994). We thus include $\Delta P_c$ of liquid iron at ambient melting point as an extra constraint (see Figure 1b). The resulting $\Delta P_c$ is expressed by a sigmoid function as

$$\Delta P_c = \frac{17.38}{1 + \exp((\rho - 11.395) \cdot 1.341)}. \quad (6)$$

Here $\Delta P_c$ is in the unit of GPa, $\rho$ is in the unit of g/cm$^3$. This pressure correction is significant at low densities (about 17 GPa between 7.0 g/cm$^3$ and 9.0 g/cm$^3$) yet becomes less than 1 GPa beyond 13.5 g/cm$^3$, indicating the accuracy of ab initio simulations improves at high densities. The corresponding correction to the internal energy is

$$\Delta U_c = -\int_{V_0}^{V} \Delta P_c dV. \quad (7)$$

We perform two sets of fitting: one with the original AIMD data ($U_n, P_n, V_n, T_n$), the other with $U_n$ and $P_n$ shifted to $U_n + \Delta U_c(V_n)$ and $P_n + \Delta P_c(V_n)$. The first set of fitting corresponds to the original ab initio results (see supplemental), the second corresponds to an improved version that can be applied directly. Unless specified explicitly, our results and discussion will be based on the second set of fitting, where the uncertainties associated with *ab initio* simulations have been compensated.

## 5. Thermal Properties of Liquid Iron

Figures 2a and 2b show the fittings of corrected internal energies and pressures. The resulting parameters for $F(V, T)$ are tabulated in Table 1 with fitting errors shown in Figures 2c and 2d. These errors are fairly small considering the volume and temperature range involved. Comparing to Wagle and Steinle-Neumann (2019) the fitting errors were reduced by an

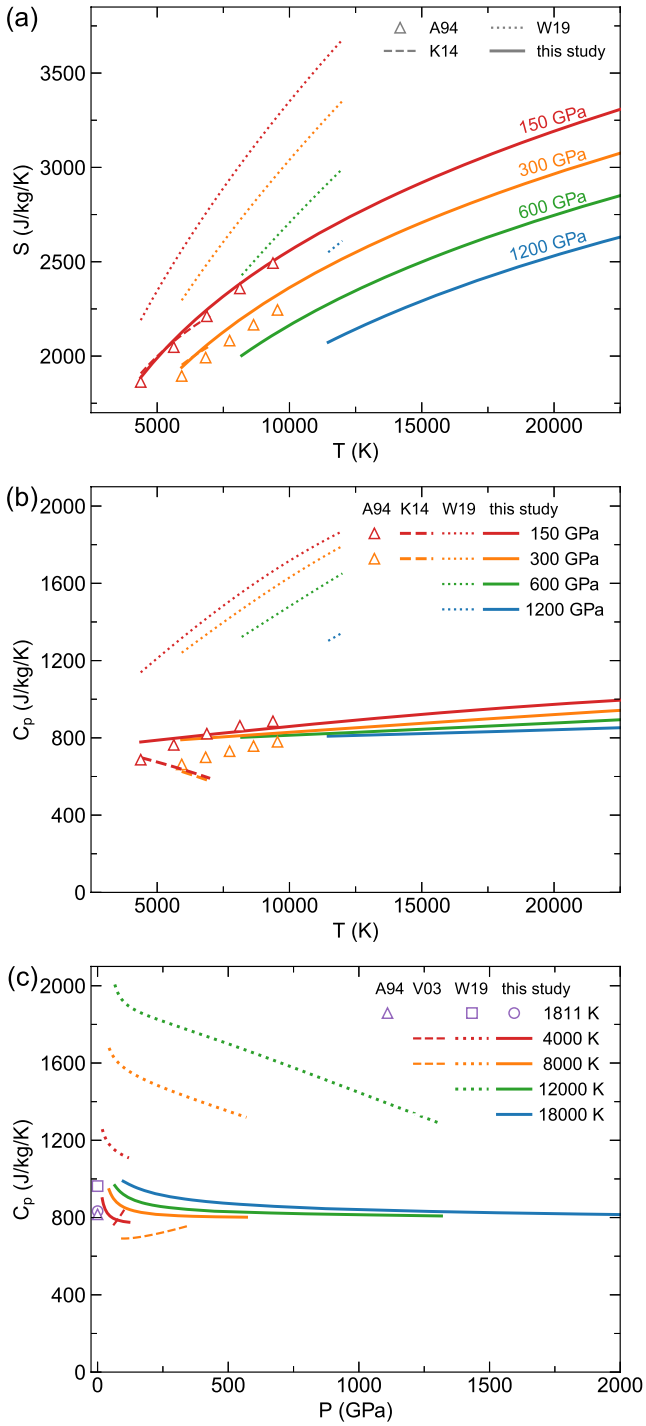


**Figure 6.** (a) Entropy of liquid iron as a function of temperature. (b) Isobaric heat capacity of liquid iron as a function of temperature. (c) Isobaric heat capacity of liquid iron as a function of pressure at representative temperatures. "A94" denotes thermal properties of liquid iron from the reduced shock data by Anderson and Ahrens (1994). "K14" denotes the results of thermodynamic modeling by Komabayashi (2014). "V03" and "W19" denote the density functional theory results for liquid iron by Vočadlo et al. (2003) and Wagle and Steinle-Neumann (2019).

order of magnitude. The small fitting errors indicate that our AIMD calculations are well-converged and thermodynamic modeling based on Equation 2 is appropriate.

Once $F(V, T)$ is determined, the EoS $P(V, T)$ can be evaluated via $-(\partial F/\partial V)_T$. Figure 3a compares the calculated EoS with DAC measurements (Kuwayama et al., 2020). Although the original ab initio EoS (labeled as "uncor.") underestimates pressure by about 17 GPa, the EoS after pressure shift (labeled as "cor.") agrees very well with the DAC measurements. Indeed, the agreement is comparable to the EoS constructed by Kuwayama et al. (2020) themselves (see the inset of Figure 3a). However, the EoS of Kuwayama et al. (2020) extrapolated to higher $P$-$T$ differs substantially from our EoS, with the latter in close agreement with the reduced shock wave data of Anderson and Ahrens (1994), as shown in the inset of Figure 3b. Kuwayama et al. (2020) had postulated that temperatures in Anderson and Ahrens (1994) were substantially overestimated; the present calculations suggest otherwise.

To clarify this issue, we calculate the shock Hugoniot using the Rankin-Hugoniot equation

$$U_h = U_{h0} + \frac{1}{2}(P_h + P_{h0})(V_{h0} - V_h), \tag{8}$$

where $U_h$, $P_h$, $V_h$ are the internal energy, pressure, and volume along the Hugoniot curve, $U_{h0}$, $P_{h0}$ and $V_{h0}$ are those of the starting point, the body-centered cubic (bcc) iron at ambient pressure and temperature. Instead of dealing with bcc iron directly, we started with the internal energy of liquid iron at ambient melting point, then added the experimentally measured enthalpy difference ($1.3 \times 10^6$ J/kg) (Anderson & Ahrens, 1994) to determine the $U_{h0}$ of bcc iron. The results are shown in Figure 4. The theoretical Hugoniot agree well with experiments up to 1 TPa and 25000 K (Al'tshuler et al., 1962, 1996; Anderson & Ahrens, 1994; Brown et al., 2000; Brown & Mcqueen, 1986; Sakaiya et al., 2014). Our calculations confirm previous reports (Vočadlo et al., 2003) that the Hugoniot temperature in Brown and Mcqueen (1986) was overestimated, yet this overestimation has largely been corrected in the refined analysis of Anderson and Ahrens (1994). At 12.64 g/cm$^3$, the Hugoniot temperature determined by Brown and Mcqueen (1986), Anderson and Ahrens (1994), and the present study is 6922 K, 5871 K, and 5877 K, respectively. The discrepancy between the EoS of Kuwayama et al. (2020) and Anderson and Ahrens (1994) is mainly due to the uncertainties associated with extrapolation of DAC data, rather than overestimation of Hugoniot temperature.

Comparing to previous DFT calculations, the present EoS agrees with that of Wagle and Steinle-Neumann (2019) at low $P$-$T$. At high $P$-$T$ they deviate substantially, as shown in Figure 3b. The discrepancy is partly due to a flaw in Wagle and Steinle-Neumann 's modeling (see supplemental). Also, Wagle and Steinle-Neumann (2019) used a PAW potential containing 14 valence electrons only. As density or temperature increases, the minimal interatomic distance decreases and the effect of 3$s$ semi-core electrons becomes non-negligible. To get accurate thermal properties of liquid iron in a wide $P$-$T$ range, it is essential to use pseudopotentials with 16 valence electrons (Li et al., 2021; Sjostrom & Crockett, 2018).

After considering the first order derivative of free energy, $P(V, T)$, we now inspect higher order properties. We start with thermal expansivity $\alpha$, defined as $\alpha \equiv -1/\rho(\partial\rho/\partial T)_p$. Figure 5a shows the isobars of liquid iron at four repre-

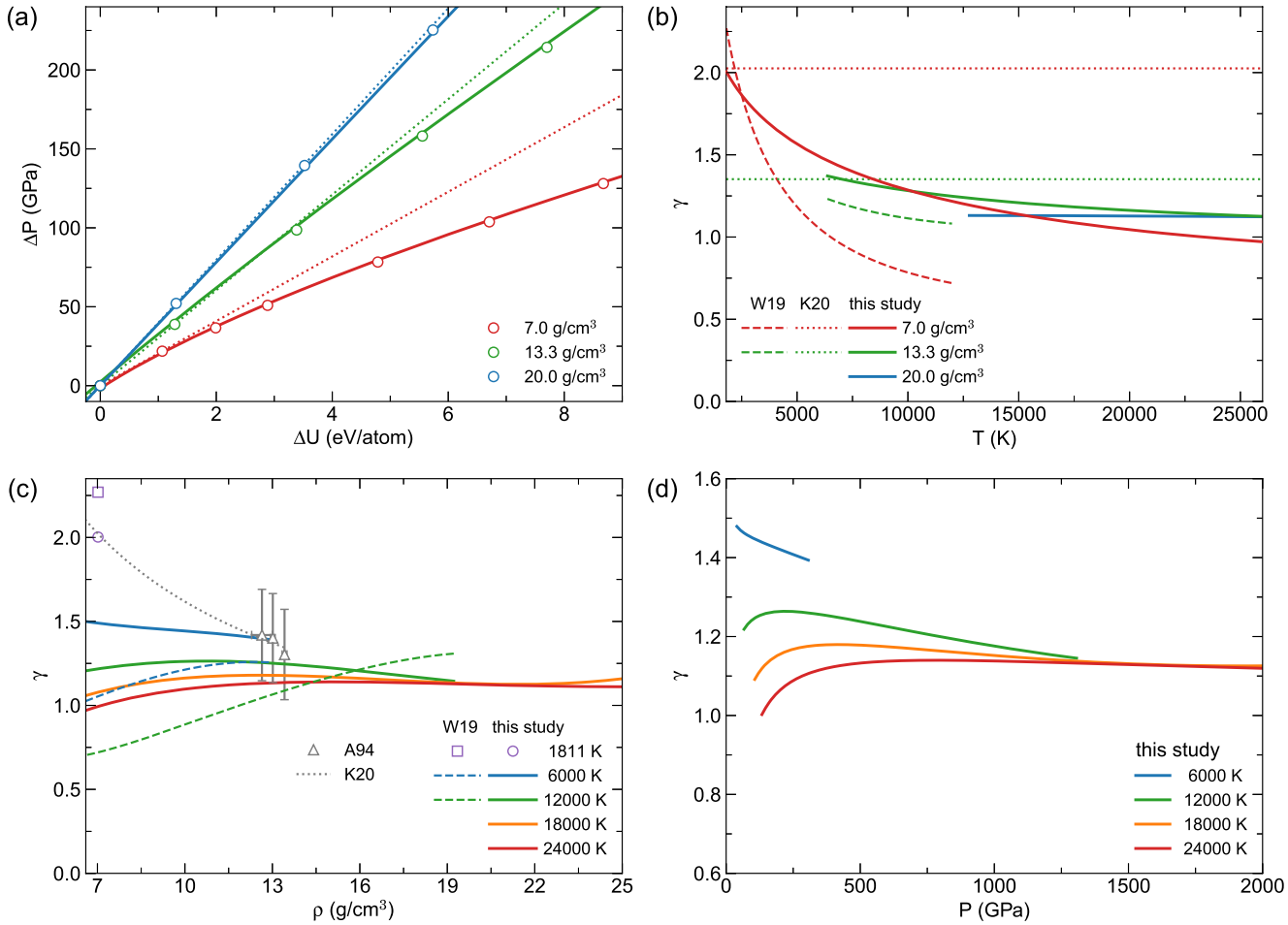


**Figure 7.** (a) Pressure ($P$) of liquid iron as a function of internal energy ($U$) at representative densities. For clearer comparison they are shifted respect to the $P$ and $U$ at the lowest simulation temperature: 1800 K for 7.0 g/cm$^3$: 7000 K for 13.3 g/cm$^3$, 12000 K for 20.0 g/cm$^3$. (b) Grüneisen parameter of liquid iron at representative densities. (c) Grüneisen parameter of liquid iron as a function of density. (d) Grüneisen parameter of liquid iron as a function of pressure. "A94" denotes Grüneisen parameters originally measured by Brown and Mcqueen (1986) and later refined by Anderson and Ahrens (1994), "K20" from the diamond anvil cell experiment by Kuwayama et al. (2020). "W19" from the density functional theory calculations by Wagle and Steinle-Neumann (2019).

sentative pressures. The corresponding isobars of hcp iron (Hakim et al., 2018) are also plotted as references. Upon melting, the density exhibits a small jump, and the magnitudes of this jump predicted by our calculations and those of Wagle and Steinle-Neumann (2019) are similar. However, the liquid density predicted by Wagle and Steinle-Neumann (2019) decreases more rapidly with $T$, resulting in a much higher $\alpha$. By contrast, our predicted $\alpha$ are consistent with the thermodynamic modeling by Komabayashi (2014), the reduced shock data (Anderson & Ahrens, 1994) as well as other DFT simulations (Vočadlo et al., 2003). The good agreement with these relatively low $P$-$T$ studies validates our approach, and lends support to our predictions in the higher $P$-$T$ regime. As shown in Figures 5b and 5c, our calculated $\alpha$ is nearly $T$-independent. It decreases rapidly with pressure at low $P$, from $10.9 \times 10^{-5}$ K$^{-1}$ at 0 GPa to $2.5 \times 10^{-5}$ K$^{-1}$ at 100 GPa. It then decreases slowly with $P$, reaching $0.5 \times 10^{-5}$ K$^{-1}$ at 1 TPa. Notably, the values of $\alpha$ we predicted for liquid iron are close to those of hcp iron (Hakim et al., 2018) near the melting temperature, which may be related to the fact that they are both close packed structures with similar coordination numbers (Alfè et al., 2000).

We now move to the isobaric heat capacity, which is related to the entropy of the system as $C_p \equiv T\,(\partial S/\partial T)_p$. As shown in Figure 6a, entropies from our calculations are in good agreement with those reduced from shock wave measurements (Anderson & Ahrens, 1994), whereas substantially lower than those of Wagle and Steinle-Neumann (2019). At the ambient melting point (7.02 g/cm$^3$, 1811 K), the entropy we get is 100.9 J/mol/K (1804.9 J/kg/K), in excellent agreement with the experimental value 99.8 J/mol/K (Chase, 1998). By contrast, the entropy

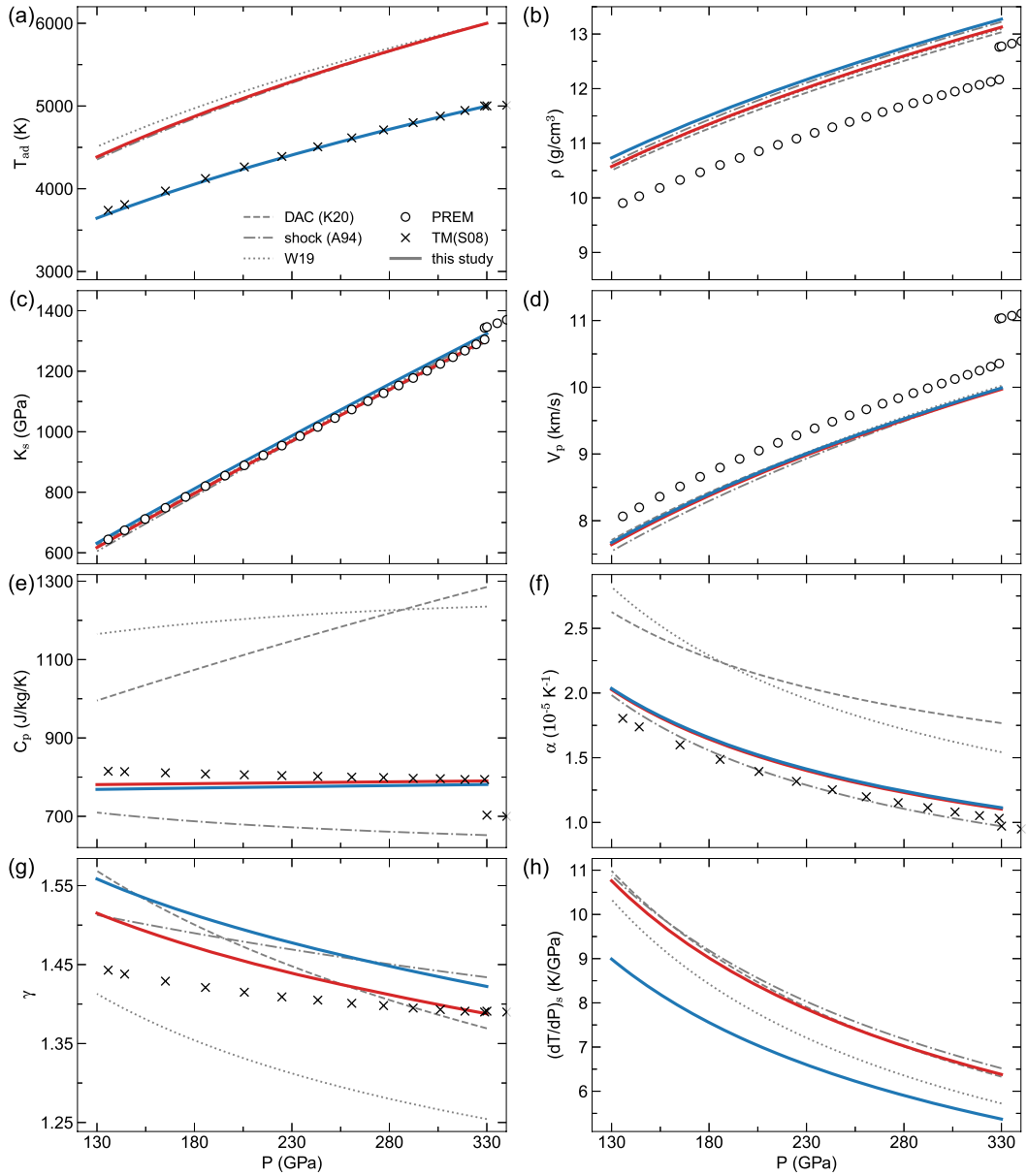


**Figure 8.** Thermal properties of liquid iron at conditions of the Earth's outer core. (a) The isentropic temperature profile with $T_{ICB}$ = 6000 K (red line) and $T_{ICB}$ = 5000 K (blue line). (b) Density, (c) adiabatic bulk modulus, (d) sound velocity, (e) isobaric heat capacity, (f) thermal expansivity, (g) Grüneisen parameter, (h) adiabatic slope along the isentropic temperature profiles. "DAC (K20)" denotes thermal properties of liquid iron from the DAC experiments by Kuwayama et al. (2020), "shock (A94)" from the reduced shock data by Anderson and Ahrens (1994), "W19" from the density functional theory calculations by Wagle and Steinle-Neumann (2019), "PREM" represents the Preliminary Reference Earth Model from seismology by Dziewonski and Anderson (1981), "TM(S08)" represents the Thermal Earth model proposed by Stacey and Davis (2008).

predicted by Wagle and Steinle-Neumann (2019) is 118.8 J/mol/K, nearly 20% higher. The differences in the $C_p$ are even greater: those from Wagle and Steinle-Neumann (2019) depend strongly on temperature and at high $T$ can exceed 1500 J/kg/K, whereas our predictions exhibit much milder temperature and pressure dependences, consistent with experimental observation (Savvatimskiy & Onufriev, 2018). In the whole $P$-$T$ regime $C_p$ is not very different from its value at the ambient melting point (837.3 J/kg/K). In prior modelings of planetary cores (Gaidos et al., 2010), the $C_p$ of liquid iron was approximated to be 850 J/kg/K. Such an approximation is validated by the present study.

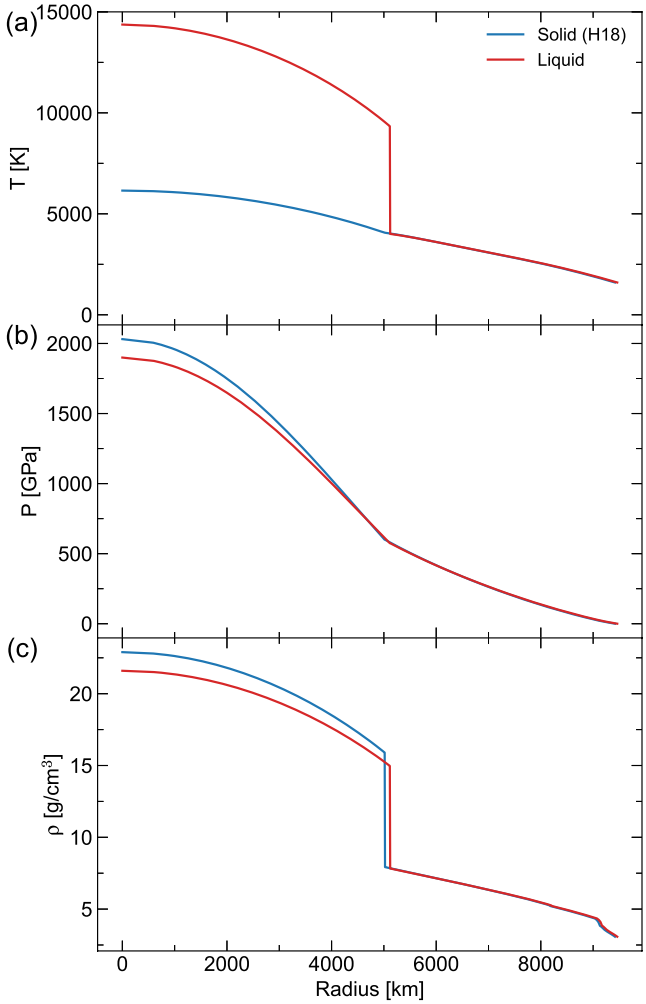


**Figure 9.** (a) Temperature, (b) pressure, (c) density profiles of the exoplanet Kepler-36b assuming an Earth-like chemical composition in the presence of a completely molten ("liquid") or frozen ("solid (H18)") core. Profiles in the molten core are derived from the thermal properties of liquid iron calculated by the present study. Profiles in the frozen core are from those of hcp iron calculated by Hakim et al. (2018). In the case of a completely molten core, the temperature at the core-mantle boundary changes abruptly, indicating the presence of a thermal boundary layer where heat is predominately transferred by conduction instead of convection.

Finally we consider the Grüneisen parameter $\gamma$, a key parameter in describing thermal properties of materials. Indeed, most experimental EoS of liquid iron are constructed in terms of $\gamma$, defined as $\gamma \equiv V\,(\partial P/\partial U)_V$. The Grüneisen parameter is also associated with the isentropic temperature profile $T_s$ as $\frac{\partial \ln T_s}{\partial \ln \rho} = \gamma$. The temperature and density dependence of $\gamma$ have been intensively studied for years, but a consensus is yet to emerge. Early experiments (Anderson & Ahrens, 1994) indicate that $\gamma$ exhibits a non-monotonic $\rho$-dependence and varies with $T$. This view was challenged by Ichikawa et al. (2014), who calculated $\gamma$ via AIMD and found no apparent $T$-dependence. Accordingly, Kuwayama et al. (2020) did not consider the temperature dependence of $\gamma$ when constructing their thermal EoS of liquid iron from DAC measurements. Ichikawa et al. (2014) conducted their simulations in a rather narrow $\rho$-$T$ range (9.34–13.01 g/cm$^3$, 4000–7000 K), which may not be adequate to fully capture the $\rho$- and $T$-dependence of $\gamma$. The substantially wider $\rho$-$T$ range explored here allows us to address this issue more clearly. As shown in Figure 7a, the $U$-$P$ curve is strongly non-linear at low densities, indicating $\gamma$ depends on $T$. At $\rho$ = 7.0 g/cm$^3$, $\gamma$ decreases from 1.98 at 1,800 K to 1.77 at 3,000 K. This $T$-dependence becomes weaker as $\rho$ increases, but is still notable at $\rho$ = 13.3 g/cm$^3$. Only at very high densities this $T$-dependence becomes negligible. Note $\gamma$ is never lower than 1.0 and approaches a constant of 1.1 in the TPa regime. This feature will be useful for determining the isentropic temperature profiles of liquid planetary cores.

## 6. Applications

We have determined thermal properties of liquid iron in a wide pressure and temperature regime. In the following we apply them to address some pending questions in planetary science. We start with the Earth's outer core, the most studied planetary core at the moment. As will be shown below, surprisingly large discrepancies exist on basic properties including heat capacity and thermal expansivity. Our results help to resolve these discrepancies. We then consider a representative massive exoplanet, Kepler-36b, to see how a completely molten core may affect its pressure and temperature profiles. Finally we discuss how the crystallization of planetary cores proceeds by comparing the melting and adiabatic slopes along the iron melting line.

The Earth's outer core is under vigorous convection as evident in the sustained geodynamo generating the Earth's magnetic field (Buffett, 2000). Accordingly, its temperature profile follows an isentropic line. This isentropic line is constrained by the temperature at the inner-core boundary (ICB) $T_{\rm ICB}$. The exact value of $T_{\rm ICB}$ is still uncertain. Here we set $T_{\rm ICB}$ = 6000 K, which implicitly assumes that light elements in the core do not strongly suppress the melting temperature (Wang et al., 2021). For completeness we also consider $T_{\rm ICB}$ = 5000 K as a lower bound and calculate the thermal properties along these two isentropic lines, as shown in Figure 8. We see that different models give similar results for the isentropic temperature $T_s$, the density $\rho$, the adiabatic bulk modulus $K_s$ and the bulk velocity $V_p$, whereas large discrepancies exist in $C_p$ and $\alpha$. Our results are close to the thermal model by Stacey and Davis (2008), but are about 50% lower than more recent studies of Wagle and Steinle-Neumann (2019) and Kuwayama et al. (2020). As shown in the Supporting Information S1, Wagle and Steinle-Neumann (2019) incorrectly modeled the internal energy of the system, leading to abnormally high $\alpha$ and $C_p$. The results of Kuwayama et al. (2020) are close to ours at low pressures where the actual measurements were conducted. The greater differences at high pressures are likely due to uncertainties associated with extrapolation. Notably, the differences in $\gamma$ and $(\partial T/\partial P)_s$ are smaller than those in $C_p$ and $\alpha$ due to error cancellations.

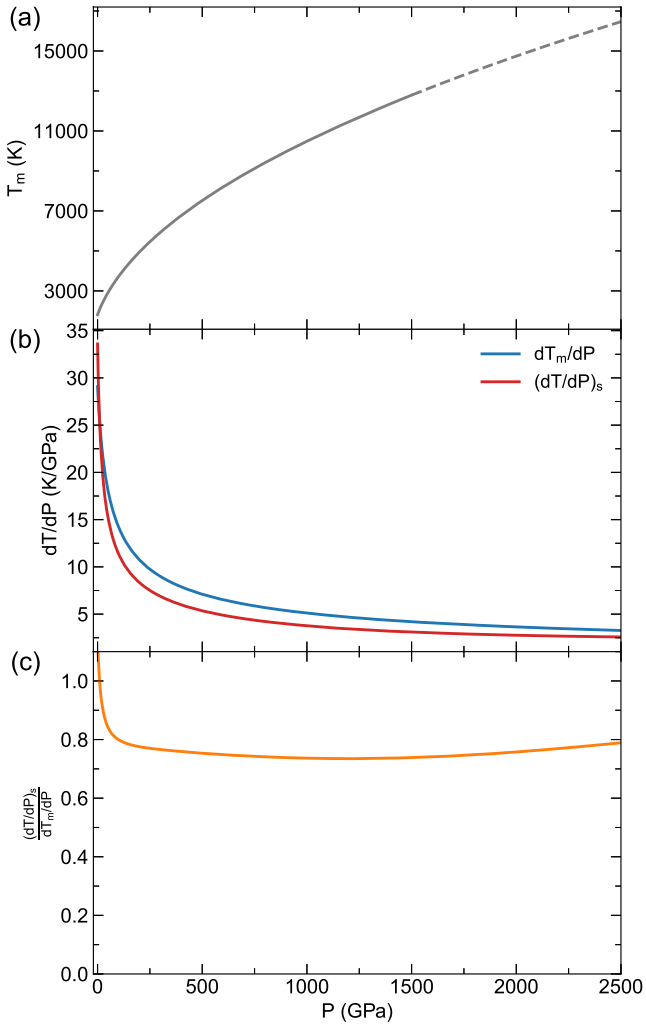


**Figure 10.** (a) Iron melting curve calculated by Bouchet et al. (2013), $T_m = 1811(P/31.3 + 1)^{1/1.99}$, with $T_m$ in the unit of Kelvin, $P$ in the unit of GPa. (b)Melting slope $dT_m/dP$ and adiabatic slope $(dT/dP)_s$ along the melting curve. (c) The ratio between the adiabatic and melting slopes.

The aforementioned properties are crucial for investigating the thermal evolution of the Earth's core. For instance, the radius of the solid inner core is approximated as (Buffett et al., 1992)

$$c(t) = b\left[\frac{\int_0^t f_m(\tau)d\tau}{\frac{2\pi}{9}b^3 C_p G\rho^2 \frac{\partial T_m}{\partial P}}\right]^{1/2}, \quad (9)$$

where $b$, $C_p$, and $\rho$ are the radius, isobaric heat capacity, and mean density of the outer core, respectively, $f_m(t)$ is the heat flux across the core-mantle boundary, $G$ is the gravitational constant, $\partial T_m/\partial P$ is the melting slope. We see that $c(t)$ is inverse proportional to $\sqrt{C_p}$. For a given $f_m(t)$, a 50% difference in $C_p$ will cause a 20% change in the rate of inner core growth. It is therefore important to get these properties as accurate as possible.

We now move to higher $P$-$T$ conditions and consider the cores of massive rocky exoplanets. Unterborn and Panero (2019) explored exoplanets of various sizes and established the upper limits of their internal pressures and temperatures. This study was conducted with the EoS of hcp iron, and it is unclear how a completely molten core may affect these limits. Here we choose Kepler-36b as a prototype to investigate this effect. Kepler-36b has a mass (4.45 Earth mass) and radius (1.486 Earth radius) more tightly constrained than most other exoplanets (Carter et al., 2012). We assume Kepler-36b has the same chemical composition as Earth, and apply the Exoplex software (Lorenzo & Unterborn, 2018; Unterborn et al., 2018) to model its interior structure. We consider two limiting cases, a completely frozen core and a completely molten core. In the first case, the isentropic temperature profile of the iron core is anchored by the temperature of the mantle at the core-mantle boundary (Hakim et al., 2018). In the second case, the isentropic temperature profile is anchored by the melting temperature of hcp iron at the center of the planet. The results are shown in Figure 9. We see that the temperature of a completely molten core can be twice that of a frozen core, whereas the core pressures are similar. This is because while the frozen core exhibits a larger density, its core radius is smaller. These two effects cancel each other, leading to a smaller change in pressure.

The above analysis assumes tacitly that crystallization of planetary cores proceeds from bottom up, just like the Earth (Higgins & Kennedy, 1971). In principle, other types of crystallization are also possible (Williams, 2009). The key quantity controlling the crystallization type is the ratio between the adiabatic slope and the melting slope. If this ratio is greater (smaller) than 1.0, then crystallization proceeds from the top-down (bottom-up), respectively. Willams (2009) and Edgington et al. (2019) compared the adiabatic slope and melting slope of iron and iron alloys and found for smaller planets such as Mercury, crystallization is likely from the top-down. The situation is unclear for massive planets. Here we calculate the adiabatic slope and the melting slope along the melting line of hcp iron, as shown in Figure 10. We see that the ratio is above 1.0 at low pressures, it then decreases rapidly with pressure up to 100 GPa, then remains a constant of ~0.8. As this ratio is much less than 1.0 at high pressures, inclusion of light elements is unlikely to change the trend. Accordingly, crystallizations of massive planetary cores are expected to proceed from the bottom-up, instead of the top-down.

## 7. Conclusions

We have calculated thermal properties of liquid iron in a wide pressure and temperature range using the formally exact ab initio thermodynamic integration method. The resulting thermal EoS agrees well with the DAC data in the $P$-$T$ range of measurements, yet deviates considerably with respect to its high $P$-$T$ extrapolations, indicating such extrapolations may require further examinations. By contrast, the present results agree well with the reduced shock wave data, confirming the validity of such measurements. Higher order thermal properties such as heat

capacity and thermal expansivity are found to be substantially lower than some recent reports, which have important ramifications for the thermal evolution of planetary cores. We also find a completely molten core can have a temperature twice that of a solid core whereas their pressures are similar. Moreover, crystallizations of massive planetary cores are likely to proceed from the bottom up. These results lay the foundation for more comprehensive studies of the thermal structure and evolution of planetary cores.

## Data Availability Statement

The data and the accompanying python codes are available in the Science Data Bank (http://doi.org/10.11922/sciencedb.o00015.00008).

**Acknowledgments**
Work at University of Chinese Academy of Sciences is supported by the Strategic Priority Research Program (B) of the Chinese Academy of Sciences (Grant No. XDB18000000) and NSFC grant No. 41972044. Work at University College London is supported by STFC grant No. ST/T000163/1. Calculations were performed on Tianhe-2 at the National Supercomputer Center of China (NSCC) in Guangzhou.

## References

Alfè, D., Kresse, G., & Gillan, M. J. (2000). Structure and dynamics of liquid iron under Earth's core conditions. *Physical Review B*, *61*, 132–142. https://doi.org/10.1103/PhysRevB.61.132

Alfè, D., Price, G. D., & Gillan, M. J. (2002). Iron under Earth's core conditions: Liquid-state thermodynamics and high-pressure melting curve from ab initio calculations. *Physical Review B*, *65*, 165118. https://doi.org/10.1103/PhysRevB.65.165118

Al'tshuler, L. V., Bakanova, A. A., & Trunin, R. F. (1962). Shock adiabats and zero isotherms of seven metals at high pressures. *Soviet Physics JETP*, *15*(1), 65–74. Retrieved from www.jetp.ac.ru to www.jetp.ras.ru

Al'tshuler, L. V., Trunin, R. F., Krupnikov, K. K., & Panov, N. V. (1996). Explosive laboratory devices for shock wave compression studies. *Physics-Uspekhi*, *39*(5), 539–544. https://doi.org/10.1070/PU1996v039n05ABEH000147

Anderson, W. W., & Ahrens, T. J. (1994). An equation of state for liquid iron and implications for the Earth's core. *Journal of Geophysical Research*, *99*, 4273–4284. https://doi.org/10.1029/93JB03158

Badro, J., Côté, A. S., & Brodholt, J. P. (2014). A seismologically consistent compositional model of Earth's core. *Proceedings of the National Academy of Sciences*, *111*, 7542–7545. https://doi.org/10.1073/pnas.1316708111

Blöchl, P. E. (1994). Projector augmented-wave method. *Physical Review B*, *50*, 17953–17979. https://doi.org/10.1103/PhysRevB.50.17953

Bonati, I., Lasbleis, M., & Noack, L. (2021). Structure and thermal evolution of exoplanetary cores. *Journal of Geophysical Research: Planets*, *126*(5), e2020JE006724. https://doi.org/10.1029/2020JE006724

Bouchet, J., Mazevet, S., Morard, G., Guyot, F., & Musella, R. (2013). Ab initio equation of state of iron up to 1500 GPa. *Physical Review B*, *87*(9), 094102. https://doi.org/10.1103/PhysRevB.87.094102

Boujibar, A., Driscoll, P., & Fei, Y. (2020). Super-Earth internal structures and initial thermal states. *Journal of Geophysical Research: Planets*, *125*, e2019JE006124. https://doi.org/10.1029/2019JE006124

Brown, J. M., Fritz, J. N., & Hixson, R. S. (2000). Hugoniot data for iron. *Journal of Applied Physics*, *88*, 5496–5498. https://doi.org/10.1063/1.1319320

Brown, J. M., & Mcqueen, R. G. (1986). Phase transitions, Grücneisen parameter, and elasticity for shocked iron between 77 GPa and 400 GPa. *Journal of Geophysical Research*, *91*, 7485–7494. https://doi.org/10.1029/JB091iB07p07485

Buffett, B. A. (2000). Earth's core and the geodynamo. *Science*, *288*, 2007–2012. https://doi.org/10.1126/science.288.5473.2007

Buffett, B. A., Huppert, H. E., Lister, J. R., & Woods, A. W. (1992). Analytical model for solidification of the Earth's core. *Nature*, *356*(6367), 329–331. https://doi.org/10.1038/356329a0

Carter, J. A., Agol, E., Chaplin, W. J., Basu, S., Bedding, T. R., Buchhave, L. A., et al. (2012). Kepler-36: A pair of planets with neighboring orbits and dissimilar densities. *Science*, *337*, 556–559. https://doi.org/10.1126/science.1223269

Chabot, N. L., Wollack, E. A., Klima, R. L., & Minitti, M. E. (2014). Experimental constraints on Mercury's core composition. *Earth and Planetary Science Letters*, *390*, 199–208. https://doi.org/10.1016/j.epsl.2014.01.004

Chase, M. W. (1998). *NIST-JANAF thermochemical tables* (4th ed.), American Institute of Physics.

dePater, I., & Lissauer, J. J. (2015). *Planetary sciences* (2nd ed.), Cambridge University Press.

Dewaele, A., Loubeyre, P., Occelli, F., Mezouar, M., Dorogokupets, P. I., & Torrent, M. (2006). Quasihydrostatic equation of state of iron above 2 Mbar. *Physical Review Letters*, *97*, 215504. https://doi.org/10.1103/PhysRevLett.97.215504

Dorogokupets, P. I., Dymshits, A. M., Litasov, K. D., & Sokolova, T. S. (2017). Termodynamics and equations of state of iron to 350 GPa and 6000 K. *Scientific Reports*, *7*, 41863. https://doi.org/10.1038/srep41863

Dziewonski, A. M., & Anderson, D. L. (1981). Preliminary reference Earth model. *Physics of the Earth and Planetary Interiors*, *25*, 297–356. https://doi.org/10.1016/0031-9201(81)90046-7

Edgington, A. L., Vočadlo, L., Stixrude, L., Wood, I. G., Dobson, D. P., & Holmström, E. (2019). The top-down crystallisation of Mercury's core. *Earth and Planetary Science Letters*, *528*, 115838. https://doi.org/10.1016/j.epsl.2019.115838

Fei, Y.-W., Murphy, C., Shibazaki, Y., Shahar, A., & Huang, H.-J. (2016). Thermal equation of state of hcp-iron: Constraint on the density deficit of Earth's solid inner core. *Geophysical Research Letters*, *43*, 6837–6843. https://doi.org/10.1002/2016GL069456

Gaidos, E., Conrad, C. P., Manga, M., & Hernlund, J. (2010). Thermodynamic limits on magnetodynamos in rocky exoplanets. *The Astrophysical Journal*, *718*(2), 596–609. https://doi.org/10.1088/0004-637X/718/2/596

Giannozzi, P., Baroni, S., Bonini, N., Calandra, M., Car, R., Cavazzoni, C., et al. (2009). QUANTUM ESPRESSO: A modular and open-source software project for quantum simulations of materials. *Journal of Physics: Condensed Matter*, *21*(39), 395502. https://doi.org/10.1088/0953-8984/21/39/395502

Grant, S. C., Ao, T., Seagle, C. T., Porwitzky, A. J., Davis, J.-P., Cochrane, K. R., et al. (2021). Equation of state measurements on iron near the melting curve at planetary core conditions by shock and ramp compressions. *Journal of Geophysical Research: Solid Earth*, *126*, e2020JB020008. https://doi.org/10.1029/2020JB020008

Hakim, K., Rivoldini, A., Van Hoolst, T., Cottenier, S., Jaeken, J., Chust, T., & Steinle-Neumann, G. (2018). A new ab initio equation of state of hcp-Fe and its implication on the interior structure and mass-radius relations of rocky super-Earths. *Icarus*, *313*, 61–78. https://doi.org/10.1016/j.icarus.2018.05.005

Heyes, D. M., & Okumura, H. (2006). Equation of state and structural properties of the Weeks-Chandler-Andersen fluid. *The Journal of Chemical Physics*, *124*(16), 164507. https://doi.org/10.1063/1.2176675

Higgins, G., & Kennedy, G. C. (1971). The adiabatic gradient and the melting point gradient in the core of the Earth. *Journal of Geophysical Research*, *76*(8), 1870–1878. https://doi.org/10.1029/jb076i008p01870

Ichikawa, H., Tsuchiya, T., & Tange, Y. (2014). The P-V-T equation of state and thermodynamic properties of liquid iron. *Journal of Geophysical Research: Solid Earth*, *119*, 240–252. https://doi.org/10.1002/2013JB010732

Komabayashi, T. (2014). Thermodynamics of melting relations in the system Fe-FeO at high pressure: Implications for oxygen in the Earth's core. *Journal of Geophysical Research: Solid Earth*, *119*, 4164–4177. https://doi.org/10.1002/2014JB010980

Kresse, G., & Furthmüller, J. (1996). Efficiency of ab-initio total energy calculations for metals and semiconductors using a plane-wave basis set. *Computational Materials Science*, *6*(1), 15–50. https://doi.org/10.1016/0927-0256(96)00008-0

Kresse, G., & Hafner, J. (1994). Ab initio molecular-dynamics simulation of the liquid-metal-amorphous-semiconductor transition in germanium. *Physical Review B*, *49*(20), 14251–14269. https://doi.org/10.1103/PhysRevB.49.14251

Kresse, G., & Joubert, D. (1999). From ultrasoft pseudopotentials to the projector augmented-wave method. *Physical Review B*, *59*(3), 1758–1775. https://doi.org/10.1103/PhysRevB.59.1758

Kuwayama, Y., Morard, G., Nakajima, Y., Hirose, K., Baron, A. Q. R., Kawaguchi, S. I., et al. (2020). Equation of state of liquid iron under extreme conditions. *Physical Review Letters*, *124*, 165701. https://doi.org/10.1103/PhysRevLett.124.165701

Li, Q., Sun, T., Zhang, Y.-G., Xian, J.-W., & Vočadlo, L. (2021). Atomic transport properties of liquid iron at conditions of planetary cores. *The Journal of Chemical Physics*, *155*, 194505. https://doi.org/10.1063/5.0062081

Lorenzo, A., & Unterborn, C. T. (2018). *Amloren1/ExoPlex: ExoPlex pre-release*. Zenodo. Retrieved from https://zenodo.org/record/1208161

Margot, J. L., Peale, S. J., Jurgens, R. F., Slade, M. A., & Holin, I. V. (2007). Large longitude libration of Mercury reveals a molten core. *Science*, *316*(5825), 710–714. https://doi.org/10.1126/science.1140514

Mermin, N. D. (1965). Thermal properties of the inhomogeneous electron gas. *Physical Review*, *137*, A1441–A1443. https://doi.org/10.1103/PhysRev.137.A1441

Miozzi, F., Matas, J., Guignot, N., Badro, J., Siebert, J., & Fiquet, G. (2020). A new reference for the thermal equation of state of iron. *Minerals*, *10*(2), 100. https://doi.org/10.3390/min10020100

Mirzaeinia, A., Feyzi, F., & Hashemianzadeh, S. M. (2017). Equation of state and Helmholtz free energy for the atomic system of the repulsive Lennard-Jones particles. *The Journal of Chemical Physics*, *147*(21), 214503. https://doi.org/10.1063/1.4997256

Murphy, C. A., Jackson, J. M., Sturhahn, W., & Chen, B. (2011). Melting and thermal pressure of hcp-Fe from the phonon density of states. *Physics of the Earth and Planetary Interiors*, *188*, 114–120. https://doi.org/10.1016/j.pepi.2011.07.001

Nosé, S. (1984). A unified formulation of the constant temperature molecular dynamics methods. *The Journal of Chemical Physics*, *81*(1), 511–519. https://doi.org/10.1063/1.447334

Perdew, J. P., Burke, K., & Ernzerhof, M. (1996). Generalized gradient approximation made simple. *Physical Review Letters*, *77*(18), 3865–3868. https://doi.org/10.1103/PhysRevLett.77.3865

Rubie, D. C., Nimmo, F., & Melosh, H. J. (2015). 9.03 - Formation of the Earth's core. In *Treatise on geophysics* (Ed.) In G. Schubert (Ed.), (2nd ed., Vol. 9, pp. 43–79). Elsevier. https://doi.org/10.1016/B978-0-444-53802-4.00154-8

Sakaiya, T., Takahashi, H., Kondo, T., Kadono, T., Hironaka, Y., Irifune, T., & Shigemori, K. (2014). Sound velocity and density measurements of liquid iron up to 800 GPa: A universal relation between Birch's law coefficients for solid and liquid metals. *Earth and Planetary Science Letters*, *392*, 80–85. https://doi.org/10.1016/j.epsl.2014.02.019

Savvatimskiy, A. I., & Onufriev, S. V. (2018). Specific heat of liquid iron from the melting point to the boiling point. *High Temperature*, *56*, 933–935. https://doi.org/10.1134/S0018151X18060202

Sjostrom, T., & Crockett, S. (2018). Quantum molecular dynamics of warm dense iron and a five-phase equation of state. *Physical Review E*, *97*, 053209. https://doi.org/10.1103/PhysRevE.97.053209

Smith, R. F., Fratanduono, D. E., Braun, D. G., Duffy, T. S., Wicks, J. K., Celliers, P. M., et al. (2018). Equation of state of iron under core conditions of large rocky exoplanets. *Nature Astronomy*, *2*, 452–458. https://doi.org/10.1038/s41550-018-0437-9

Stacey, F. D., & Davis, P. M. (2008). *Physics of the Earth* (4th ed.), Cambridge University Press. https://doi.org/10.1017/CBO9780511812910.003

Stähler, S. C., Khan, A., Banerdt, W. B., Lognonné, P., Giardini, D., Ceylan, S., et al. (2021). Seismic detection of the martian core. *Science*, *373*, 443–448. https://doi.org/10.1126/science.abi7730

Stixrude, L. (2014). Melting in super-Earths. *Philosophical Transactions of the Royal Society A*, *372*, 20130076. https://doi.org/10.1098/rsta.2013.0076

Sun, T., Brodholt, J. P., Li, Y.-G., & Vočadlo, L. (2018). Melting properties from ab initio free energy calculations: Iron at the Earth's inner-core boundary. *Physical Review B*, *98*, 224301. https://doi.org/10.1103/PhysRevB.98.224301

Umemoto, K., & Hirose, K. (2020). Chemical compositions of the outer core examined by first principles calculations. *Earth and Planetary Science Letters*, *531*, 116009. https://doi.org/10.1016/j.epsl.2019.116009

Unterborn, C. T., Desch, S. J., Hinkel, N. R., & Lorenzo, A. (2018). Inward migration of the TRAPPIST-1 planets as inferred from their water-rich compositions. *Nature Astronomy*, *2*, 297–302. https://doi.org/10.1038/s41550-018-0411-6

Unterborn, C. T., & Panero, W. R. (2019). The pressure and temperature limits of likely rocky exoplanets. *Journal of Geophysical Research: Planets*, *124*, 1704–1716. https://doi.org/10.1029/2018JE005844

Vočadlo, L., Alfè, D., Gillan, M. J., & Price, G. D. (2003). The properties of iron under core conditions from first principles calculations. *Physics of the Earth and Planetary Interiors*, *140*(1), 101–125. https://doi.org/10.1016/j.pepi.2003.08.001

Wagle, F., & Steinle-Neumann, G. (2019). Liquid iron equation of state to the terapascal regime from ab initio simulations. *Journal of Geophysical Research: Solid Earth*, *124*, 3350–3364. https://doi.org/10.1029/2018JB016994

Wang, W., Li, Y., Brodholt, J. P., Vočadlo, L., Walter, M. J., & Wu, Z. (2021). Strong shear softening induced by superionic hydrogen in Earth's inner core. *Earth and Planetary Science Letters*, *568*, 117014. https://doi.org/10.1016/j.epsl.2021.117014

Waseda, Y., & Suzuki, K. (1970). Atomic distribution and magnetic moment in liquid iron by neutron diffraction. *Physics, chemistry and metallurgy*, *39*, 669–678. https://doi.org/10.1002/pssb.19700390235

Williams, Q. (2009). Bottom-up versus top-down solidification of the cores of small solar system bodies: Constraints on paradoxical cores. *Earth and Planetary Science Letters*, *284*(3), 564–569. https://doi.org/10.1016/j.epsl.2009.05.019